Applied Surface Science 440 (2018) 730–740

Contents lists available at ScienceDirect

Applied Surface Science

journal homepage: www.elsevier.com/locate/apsusc

Full Length Article

Amphiphilic ligand exchange reaction-induced supercapacitor electrodes with high volumetric and scalable areal capacitances

Donghyeon Nam, Yeongbeom Heo, Sanghyuk Cheong, Yongmin Ko *, Jinhan Cho *

Department of Chemical & Biological Engineering, Korea University, 145 Anam-ro, Seongbuk-gu, Seoul 02841, Republic of Korea

ARTICLE INFO

Article history:
Received 28 August 2017
Revised 26 December 2017
Accepted 18 January 2018
Available online 31 January 2018

Keywords:
Supercapacitor
Amphiphilic ligand exchange
Multi-walled carbon nanotubes
Oleic-acid-stabilized iron oxide
PEDOT:PSS

ABSTRACT

We introduce high-performance supercapacitor electrodes with ternary components prepared from consecutive amphiphilic ligand-exchange-based layer-by-layer (LbL) assembly among amine-functionalized multi-walled carbon nanotubes (NH_2-MWCNTs) in alcohol, oleic acid-stabilized Fe_3O_4 nanoparticles (OA-Fe_3O_4 NPs) in toluene, and semiconducting polymers (PEDOT:PSS) in water. The periodic insertion of semiconducting polymers within the (OA-Fe_3O_4 NP/NH_2-MWCNT)$_n$ multilayer-coated indium tin oxide (ITO) electrode enhanced the volumetric and areal capacitances up to 408 ± 4 F cm^{-3} and 8.79 ± 0.06 mF cm^{-2} at 5 mV s^{-1}, respectively, allowing excellent cycling stability (98.8% of the initial capacitance after 5000 cycles) and good rate capability. These values were higher than those of the OA-Fe_3O_4 NP/NH_2-MWCNT multilayered electrode without semiconducting polymer linkers (volumetric capacitance ~241 ± 4 F cm^{-3} and areal capacitance ~1.95 ± 0.03 mF cm^{-2}) at the same scan rate. Furthermore, when the asymmetric supercapacitor cells (ASCs) were prepared using OA-Fe_3O_4 NP- and OA-MnO NP-based ternary component electrodes, they displayed high volumetric energy (0.36 mW h cm^{-3}) and power densities (820 mW cm^{-3}).

1. Introduction

Since the beginning of this century, the rapid growth and evolution of various portable electronics, microelectronic systems, and electronic motor vehicles has continuously increased the need for the development of high-energy renewable energy-storage sources (e.g., supercapacitors, batteries, and fuel cells) [1–6]. Among these various energy-storage devices, supercapacitors are an important energy-storage component of high-power applications due to their higher power density (>10 kW kg^{-1}) and longer operation lifetimes than batteries and, additionally, their simpler and more cost-effective structure than fuel cells [1–4,7–10]. However, the energy density of supercapacitors (approximately 5 W h kg^{-1}) is considerably lower than that of batteries (approximately 150 W h kg^{-1}), which serves as a critical obstacle in the replacement of battery-based electronics with supercapacitor-based electronics. Therefore, much more effort has been directed toward the development of supercapacitors with high-capacitance performance closely related to the energy density.

To enhance the energy density of supercapacitors, a variety of pseudocapacitive nanoparticles (PC NPs), such as RuO_x, MnO_x, Fe_3O_4, and WO_x, with high specific capacitance have been incorporated into conductive carbon-based materials (i.e., multi-walled carbon nanotubes (MWCNTs), reduced graphene oxides (r-GOs), and porous carbons) and/or conducting (or semiconducting) polymer matrices through various physical adsorption processes (e.g., dip coating, Meyer rod coating, and dispensing writing) [11–14]. However, these approaches have difficulty increasing the PC NP loading amount within the electrodes due to NP aggregation. Furthermore, the unstable interface interactions (i.e., physical adsorption) between conductive matrices and PC NPs have limited the long-term operation of the electrodes.

Recently, layer-by-layer (LbL) assembly using complementary interactions (i.e., electrostatic, hydrogen bonding, and covalent bonding interactions) between two different components has been demonstrated as an effective process to fabricate thin-film electrodes with controlled loading amounts, thicknesses, structures, and compositions of the active materials irrespective of the substrate size or shape [9–11,15–19,24–26]. Additionally, supercapacitor electrodes based on LbL assembly, in comparison with those electrodes prepared from other conventional methods, can significantly enhance the areal capacitance that is considered a practical performance parameter for energy-storage devices [9,10,15–19]. Hyder et al. reported that the total charges of (cationic TiO_2 NP/anionic MWCNT)$_n$ electrodes can be enhanced by increasing the

* Corresponding authors.
E-mail addresses: radiofeel@korea.ac.kr (Y. Ko), jinhan71@korea.ac.kr (J. Cho).

https://doi.org/10.1016/j.apsusc.2018.01.153
0169-4332/

bilayer number (n) of the electrochemically active components using electrostatic LbL assembly [17]. Dong et al. demonstrated that the areal charge capacity of LbL-assembled (Co-Al hydroxide nanosheet/graphene)$_n$ multilayer electrodes could regularly increase with an increasing bilayer number, indicating the controllability and uniformity of the electrostatic LbL deposition process [19]. Although electrostatically charged PC NPs for LbL-assembled supercapacitor electrodes induce a low packing density per layer because of electrostatic repulsion between the same charged NPs, these previous studies strongly suggest that gaining more delicate control over various processing parameters, such as the electrode structure design, effective incorporation of active materials within the electrodes, and interface interaction among the heterogeneous active components, can improve the energy performance of supercapacitor electrodes. However, using electrostatically charged PC NPs for LbL-assembled supercapacitor electrodes to greatly enhance the volumetric and areal capacitance at the same time is very difficult because the electrostatic repulsion between the same charged neighboring NPs results in low packing density of PC NPs (<30%) [20,21].

Here, we fabricated amphiphilic LbL-assembled supercapacitor electrodes composed of amine-functionalized MWCNTs (NH_2-MWCNTs), poly(3,4-ethylenedioxythiophene) polystyrene sulfonate (PEDOT:PSS), and oleic-acid-stabilized Fe_3O_4 NPs (OA-Fe_3O_4 NPs) through a ligand exchange reaction. These electrodes exhibited high volumetric and area capacitances with good rate capabilities and high operational stabilities through the facile but delicate control over their reciprocal interface interaction, ligand exchange, and active component loading amount. A main advantage of the amphiphilic LbL-assembled electrode using ternary components was that the additional incorporation of hydrophilic semiconducting polymers into the (OA-Fe_3O_4 NP/NH_2-MWCNT)$_n$ electrodes improved charge transfer and further increased the loading amount of high-energy Fe_3O_4 NPs due to the formation of a large number of adsorption sites for the Fe_3O_4 NPs. The bulky OA ligands loosely bound to the Fe_3O_4 NP surface were replaced by the NH_2 groups of the MWCNTs and sulfonic acid (SO_3^-) groups of PEDOT:PSS during the LbL deposition due to the higher affinity of the Fe_3O_4 NP surface to NH_2 and SO_3^- groups. These ternary component electrodes (i.e., (PEDOT:PSS/OA-Fe_3O_4 NP/NH_2-MWCNT/OA-Fe_3O_4 NP)$_n$, hereafter referred to as TC_n electrodes) exhibited remarkable volumetric capacitance up to 408 ± 4 F cm^{-3} at a scan rate of 5 mV s^{-1}, which was approximately 1.7 and 6.4 times higher than those of (OA-Fe_3O_4 NP/NH_2-MWCNT)$_n$ and (NH_2-MWCNT/COOH-MWCNT)$_n$ multilayers, respectively. Additionally, when the periodic layer number (n) was increased to 10, the areal capacitance of the TC_{10} electrode reached 8.79 ± 0.06 mF cm^{-2}, which was approximately 4.5 times higher than that of (OA-Fe_3O_4 NP/NH_2-MWCNT)$_{10}$. These TC_n electrodes also displayed excellent operational stability (98.8% of the initial capacitance after 5000 cycles) due to the multidentate bonding between PEDOT:PSS and the Fe_3O_4 NPs and between the MWCNTs and Fe_3O_4 NPs after amphiphilic ligand exchange. Furthermore, when the asymmetric supercapacitor cells (i.e., TC-ASCs) were prepared using OA-Fe_3O_4 NP- and OA-MnO NP-based ternary component electrodes, they exhibited the high volumetric energy density of ~0.36 mW h cm^{-3} (power density ~330 mW cm^{-3}) at a current density of 1.1 A cm^{-3}, and power density of ~820 mW cm^{-3} (energy density ~0.12 mW h cm^{-3}) at a current density of 10.3 A cm^{-3}. Considering that amphiphilic LbL assembly using ternary active components can effectively enhance the capacitance of electrodes with good rate capability and high operation stability, our approach can provide an important tool to design electrode structures and interfacial stability for high-performance energy-storage devices.

2. Experimental details

2.1. Materials

An aqueous solution of 1 mg ml^{-1} PEDOT:PSS (M_w = 70 000, Aldrich) was used as an anionic polyelectrolyte. OA-Fe_3O_4 NPs with diameter of 8 nm in toluene were synthesized by high-temperature reaction of mixture composed of iron(III) acetylacetonate (2 mmol), benzyl ether (20 ml), 1,2-hexadecandiol (10 mmol), oleic acid (5 mmol), and oleylamine (6 mmol) under nitrogen (N_2) conditions [22]. Briefly, the mixture was heated to 200 °C for 2 h, and then to ~300 °C with refluxing for 1 h. Ethanol was then added to precipitate the black-colored resultant, which was separated from the solvent using centrifugation. The black resultant was dissolved in hexane with 0.05 ml of oleic acid and oleylamine and purified with ethanol using centrifugation three times. The resulting black power was re-dispersed into toluene.

OA-MnO NPs were prepared by thermal decomposition of Mn-oleate complex [23]. In a typical synthesis, Mn-oleate complex was firstly prepared by heating a mixture of manganese(II) chloride tetrahydrate (40 mmol) and sodium oleate (80 mmol) in co-solvent of ethanol (30 ml), de-ionized water (70 ml), and *n*-hexane (70 ml) at 70 °C for 12 h under argon condition. The synthesized Mn-oleate (2 mmol) was dispersed in 1-hexadecene (12.8 ml) at 70 °C for 1 h, and heated the mixture up to 280 °C with heating rate of 2 °C min^{-1}. After 10 min at 280 °C, the black mixture was cooled and washed out using centrifugation with de-ionized water for three times. All chemicals used in the synthesis of the PC NPs (i.e., OA-Fe_3O_4 and OA-MnO) were purchased from Sigma-Aldrich.

COOH-MWCNTs and NH_2-MWCNTs) were prepared by surface modification of pristine MWCNTs (>95% purity, outer diameter ~9 nm, length ~5 μm, Aldrich) [10]. First, COOH-MWCNTs were prepared by strong acidic treatment of pristine MWCNTs with refluxing in H_2SO_4/HNO_3 mixture at 70 °C for 2 h. Then, the oxidized MWCNTs were purified with deionized water (18 MΩ cm) several times. The resulting COOH-MWCNTs (80 ml) were reacted with excess ethylenediamine (8 ml, Sigma Aldrich) and *N*-ethyl-*N*′-(3-dimethylaminopropyl)carbodiimide methiodide (800 mg, Alfar Aesar) for 5 h to prepare NH_2-MWCNTs. The resultant solution was dialyzed using membrane (MWCO ~ 12,000 to 14,000) for one week.

2.2. Build-up of the TC_n multilayers

An aqueous solution of PEDOT:PSS, toluene solution of the hydrophobic transition metal oxide (TMO) NPs (i.e., OA-Fe_3O_4 and OA-MnO NPs), and ethanol solution of the NH_2-MWCNTs were prepared at concentrations of 1, 10, and 2 mg ml^{-1}, respectively. NaCl (0.2 M) was added to the PEDOT:PSS aqueous solution. For the build-up of the LbL-assembled multilayer, a quartz or silicon substrate was first cleaned with an RCA solution (H_2O/NH_3/H_2O_2 = 5:1:1 *v/v/v*) at 60 °C. The resulting negatively charged substrates were first dipped into positively charged poly(allylamine hydrochloride) (PAH) (M_w = 70,000, Aldrich) solution with 0.2 M NaCl for 10 min, washed twice with deionized water, and sufficiently dried under a gentle air stream. The PAH-coated substrates were dipped into the PEDOT:PSS solution for 10 min, followed by washing with deionized water and thorough drying with air. The PEDOT:PSS-coated substrate was dipped into the OA-TMO NP solution for 30 min, followed by washing with toluene and drying with air. The OA-TMO NP-coated substrates were dipped into the NH_2-MWCNT solution for 10 min, followed by washing with ethanol and drying with air. Then, the substrate was dipped into the OA-TMO NP again. These dipping cycles were repeated until the desired number of periodic layers was obtained.

2.3. Measurements

A quartz crystal microbalance (QCM) device (QCM200, SRS) was used to examine the mass of the material deposited after each adsorption step. The resonance frequency of the QCM electrode was approximately 5 MHz. To prepare the TC_n multilayers on the QCM electrode, a 0.2 M NaCl PAH layer was first deposited onto the QCM electrode. Then, the adsorbed masses (Δm) of PEDOT:PSS, OA-Fe_3O_4 NPs, and NH_2-MWCNTs were calculated from the change in the QCM frequency, ΔF, using the Sauerbrey equation [25,26]:

$$\Delta F\ (\mathrm{Hz}) = -\frac{2F_0^2}{A\sqrt{\rho_q \mu_q}} \cdot \Delta m \quad (1)$$

Here, F_0 (~5 MHz) is the fundamental resonance frequency of the crystal, A is the electrode area, and ρ_q (~2.65 g cm^{-2}) and μ_q (~2.95×10^{11} g cm^{-2} s^{-2}) are the shear modulus and density of quartz, respectively. This equation can be simplified as follows:

$$-\Delta F\ (\mathrm{Hz}) = 56.6 \times \Delta m_A \quad (2)$$

where Δm_A is the mass change per quartz crystal unit area in μg cm^{-2}. In this case, we repeatedly measured (10 times) $-\Delta F$ per layer, and the resultant standard deviation of the $-\Delta F$ measurement was obtained from the same layer.

Vibrational spectra were measured by Fourier transform infrared (FTIR) spectroscopy (Agilent Technology) in specular mode. The sample chamber was purged with N_2 gas for 2 h to eliminate water and CO_2 prior to conducting the FTIR measurements. FTIR spectra for the TC_n multilayer films deposited onto Au-coated substrates were obtained using 300 scans with an incident angle of 80°. The acquired raw data were plotted after baseline correction, and the spectra were smoothed using spectrum analyzing software (OMNIC, Nicolet).

Electrochemical tests of the multilayer electrodes deposited onto PAH-coated fluorine tin oxide (FTO) electrodes were conducted using a three-electrode system, using a Ag/AgCl electrode and Pt wire as the reference and counter electrodes, respectively. The LbL-assembled electrode was employed as the working electrode in 0.1 M Na_2SO_3 electrolyte solution. Cyclic voltammetry was performed in the potential range from −0.9 to +0.1 V at scan rates of 5–400 mV s^{-1}. Electrochemical impedance spectroscopy (EIS) measurements were performed by applying an AC voltage with a 50 mV amplitude in the frequency range of 100 kHz–0.1 Hz at room temperature. The ASC electrodes for two-electrode measurement were assembled using Fe_3O_4 NP-based TC_{10} and MnO NP-based TC_{10} electrodes as a negative and positive electrodes, respectively. These positive and negative TC_{10} electrodes were integrated using a 20-μm-thick membrane (Celgard 3501) interposed between two electrodes.

The electrochemical performance of the formed multilayer electrode was evaluated using the following equation:

$$\text{Specific capacitance (C)} = \frac{\int i(V)dV}{2\upsilon\Delta V} \times \frac{1}{S} \text{ (for cyclic voltammetry)} \quad (3)$$

$$\text{Specific capacitance (C)} = \frac{I\Delta t}{\Delta V} \text{ (for galvanostatic charge-discharge measurement)} \quad (4)$$

where $i, \Delta V$, and υ correspond to the current, potential window, and scan rate, respectively. The variable S indicates the area (cm^2) or volume (cm^3) of the working electrode. The energy and power density of TC-ASCs were calculated from discharge profiles in GCD curves using follow equations:

$$\text{Energy density (E)} = 0.5CV2 \quad (5)$$

$$\text{Power density (P)} = \frac{\Delta V^2}{4R} \times \frac{1}{cell\ volume} \quad (6)$$

where R indicates the internal resistance (Ω) obtained from iR drops in GCD profiles using equation of $\Delta iR/2i$, here, i represents the applied current density.

3. Results and discussion

For the preparation of amphiphilic LbL-assembled electrodes with ternary components, anionic PEDOT:PSS in water, OA-Fe_3O_4 NPs with a diameter of approximately 8 nm in toluene (Supplementary Information, Fig. S1), and NH_2-MWCNTs in alcohol were alternately deposited onto PAH-coated substrates (Scheme 1). For the LbL assembly between PEDOT:PSS and the OA-Fe_3O_4 NPs, the SO_3^- groups of PEDOT:PSS were directly adsorbed onto the Fe_3O_4 NP surface through strong coordination bonds after OA ligand replacement. This high affinity between the SO_3^- groups of PEDOT:PSS and the Fe_3O_4 NP surface was confirmed by FTIR spectroscopy (Fig. 1a). First, the FTIR spectra of PEDOT:PSS and the OA-Fe_3O_4 NPs showed evident absorption peaks corresponding to: (1) the deformation of the phenyl ring (at 1525 and 1128 cm^{-1}), C—C thiophene ring (at 1274 cm^{-1}), ethylenedioxy group (1162 cm^{-1}), and SO_3^- stretching vibrations (at 1040 and 1010 cm^{-1}) originating from PEDOT:PSS (★) [27,28]; and (2) COO^- stretching peaks (at 1604, 1536, and 1411 cm^{-1}) derived from the OA ligands of the Fe_3O_4 NPs (▼) (Supplementary Information, Fig. S2a) [29,30]. Based on these results, we investigated the spectra of the OA ligands with increasing PEDOT:PSS deposition time onto the OA-Fe_3O_4 NP-coated substrates from 0 to 20 min (Fig. 1a). The intensity of the COO^- peaks (at 1411 and 1604 cm^{-1}) of OA ligands bound to the surface of Fe_3O_4 NPs gradually decreased, and the absorption peaks arising from PEDOT:PSS intensified. The SO_3^- groups of alkanesulfonic acid surfactants in organic media have been shown to be coordinately bonded with the Fe^{3+} sites on the surface of iron oxide NPs [31]. This previous report suggests that PEDOT:PSS containing a large number of SO_3^- groups can have a higher affinity for Fe_3O_4 NPs than OA ligands containing carboxylate ions, and thus can operate as a polymeric (or multidentate) ligand for Fe_3O_4 NPs despite the extremely different solvent polarity between the non-polar (for OA-Fe_3O_4 NPs) and aqueous media (for PEDOT:PSS) [24]. Similarly, the NH_2-MWCNTs in alcohol could be directly LbL-assembled with the OA-Fe_3O_4 NPs via ligand exchange between the NH_2 groups of the MWCNTs and the OA ligands with COO^- groups (Supplementary Information, Fig. S2b) [9]. These interfacial interactions indicate that the ternary component multilayers based on semiconducting PEDOT:PSS, pseudocapacitive Fe_3O_4 NPs, and NH_2-MWCNTs can be successfully prepared using consecutive amphiphilic ligand exchange reactions (Supplementary Information, Fig. S3).

To further confirm these phenomena, the LbL-assembled TC_n multilayers, i.e., (NH_2-MWCNT/OA-Fe_3O_4 NP/PEDOT:PSS/OA-Fe_3O_4 NP)$_n$, were sequentially deposited onto PAH-coated substrates. With an increasing periodic layer number (n) from 0 to 10, the total mass loading (by QCM) and the total thickness (by cross-sectional field-emission scanning electron microscopy (FE-SEM)) of the TC_n multilayers increased up to approximately 51.5 μg cm^{-2} and 215 nm, respectively (Fig. 1b and c). The average mass change of the OA-Fe_3O_4 NPs per layer was calculated as 2.35 μg cm^{-2}, which was considerably higher than that (i.e., average mass of the OA-Fe_3O_4 NPs per layer ~1.11 μg cm^{-2}) of the (OA-Fe_3O_4 NP/NH_2-MWCNT)$_n$ multilayers without PEDOT:PSS. These results indicate the formation of a large number of binding sites (i.e., SO_3^-) for

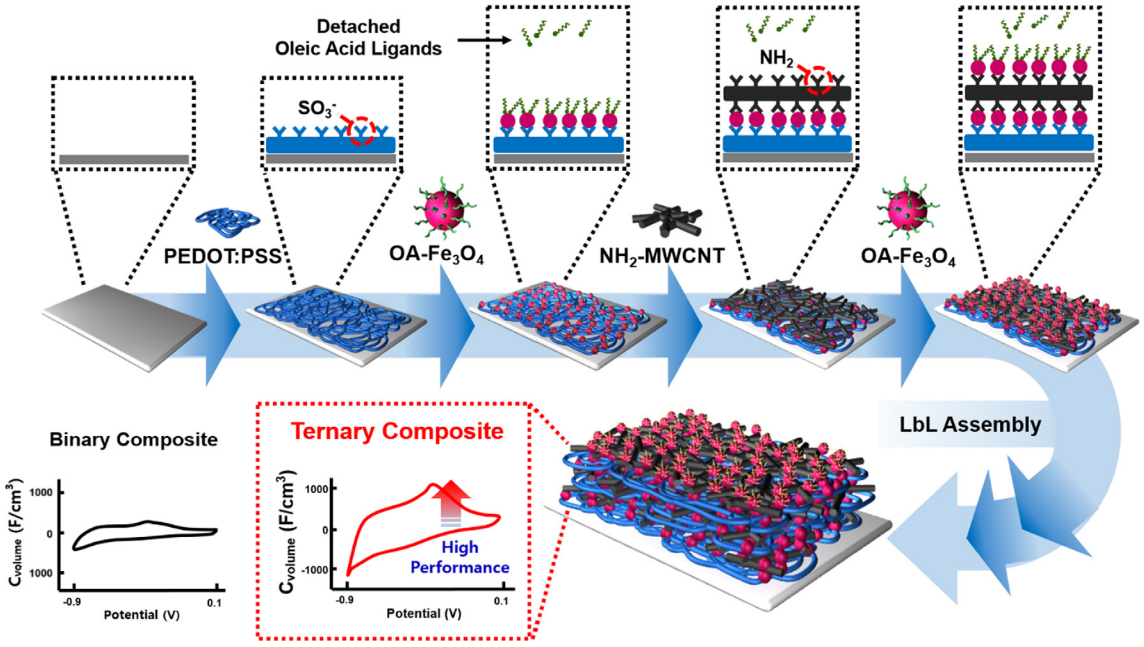

Scheme 1. Schematic representation for the ternary component multilayer electrodes using amphiphilic LbL assembly.

Fe_3O_4 NPs by the additional incorporation of PEDOT:PSS into the OA-Fe_3O_4 NP/NH_2-MWCNT multilayers. Additionally, the mass density (ρ) of the TC_n multilayers was measured to be approximately 2.42 g cm^{-3}, which was much higher than those of (OA-Fe_3O_4 NP/NH_2-MWCNT)$_n$ (ρ ~ 1.94 g cm^{-3}) and hydrogen-bonded (NH_2-MWCNT/COOH-MWCNT)$_n$ multilayers (ρ ~ 0.79 g cm^{-3}) (Supplementary Information, Fig. S4). For the (anionic Fe_3O_4 NP/cationic CNT)$_n$ multilayers prepared from traditional electrostatic LbL assembly, the mass density was approximately 1.20 g cm^{-3} due to the relatively low packing density by the electrostatic charge repulsion between the same charged Fe_3O_4 NPs. Despite the densely packed OA-Fe_3O_4 NPs within the TC_n multilayers, these multilayers exhibited a highly porous structure, possibly allowing facile charge transfer during electrochemical operation (Fig. 1d). Additionally, the ternary components (i.e., PEDOT:PSS, NH_2-MWCNTs, and OA-Fe_3O_4 NPs) were uniformly distributed within the TC_n multilayers, as confirmed by energy dispersive X-ray spectroscopy (EDX) elemental mapping (Fig. 1e). Furthermore, the active material mass loading, related to the areal performance of supercapacitor electrodes, was further scalable based on the increased periodic layer number.

On the basis of these results, we investigated the electrochemical performances of the amphiphilic LbL-assembled TC_n electrodes. For this investigation, the TC_n multilayers were first deposited onto an ITO substrate, and then their electrochemical behavior was examined in 0.1 M Na_2SO_3 electrolyte using cyclic voltammetry (CV), galvanostatic charge/discharge (GCD), and EIS measurements. Fig. 2a shows the representative electrochemical responses of the TC_n electrodes with increasing periodic number (n) from 3 to 10 at a scan rate of 50 mV s^{-1}. The non-rectangular profiles with notable redox peaks originating from the electrochemical reaction of Fe_3O_4 in the Na_2SO_3 electrolyte gradually increased with an increasing periodic number (n). These reversible redox reactions are connected with both the surface redox reaction of sulfur in form of anions (i.e., sulfate and sulfite anions) on the surface of Fe_3O_4 NPs and multivalent state change of Fe^{II} and Fe^{III} caused by the intercalation of sulfite anions [32,33]. This mechanism can be expressed as follows:

$$FeO + SO_3^{2} \leftrightarrow 5FeSO_4 + 2e^{-}$$

$$2Fe^{II}O + SO_3^{2-} \leftrightarrow (Fe^{III}O) + SO_3^{2-}(Fe^{III}O)^{+} + 2e^{-}$$

Additionally, the corresponding total charge densities linearly increased, implying that the charge capacity (or active material mass loading) can be precisely controlled by the amphiphilic LbL assembly process (the inset of Fig. 2a). These TC_n electrodes also exhibited good pseudocapacitance behaviors and double-layer capacitance behaviors in the scan rate range from 5 to 400 mV s^{-1} (Fig. 2b). These phenomena evidently showed that the amphiphilic TC_n electrodes possessed fast charge transfer, and a correspondingly good rate capability despite the high OA-Fe_3O_4 NP loading amount. Additionally, the anodic current peaks were proportional to the square root of the scan rate ($v^{1/2}$), implying that the redox reaction of the TC_n electrodes followed a diffusion-controlled process (Supplementary Fig. S5) (*more detailed explanation given later*). Interestingly, although the OA-Fe_3O_4 NPs dispersed in toluene had hydrophobic surface properties, the Fe_3O_4 NPs buried within the amphiphilic LbL-assembled multilayers exhibited hydrophilicity due to ligand exchange between the OA and SO_3^- groups of PEDOT:PSS and between the OA and NH_2 groups of the NH_2-MWCNTs. Therefore, we reasonably conclude that the hydrophobic surface properties of the OA-Fe_3O_4 NPs used for TC_n electrodes do not disturb ion transfer and diffusion in 0.1 M Na_2SO_3 electrolyte. On the other hand, an increase of scan rate induced a peak shift of the electrochemical current toward higher potentials during the anodic sweep because of the poor electrochemical reaction kinetics of the Fe_3O_4 NPs.

We also highlight that the electrochemical performance of the TC_{10} electrode outperformed those of the covalent-bonded (OA-Fe_3O_4 NP/NH_2-MWCNT)$_{10}$ (total film thickness ~81 nm) and hydrogen-bonded (NH_2-MWCNT/COOH-MWCNT)$_{10}$ electrodes (total film thickness ~105 nm) with the same periodic number at the same scan rate (Fig. 2c). Although the higher current level and larger area in the CV curve of the 215-nm-thick TC_{10} electrode are mainly attributed to the higher active material loading amount within the electrode, the comparison of the volumetric capacitance

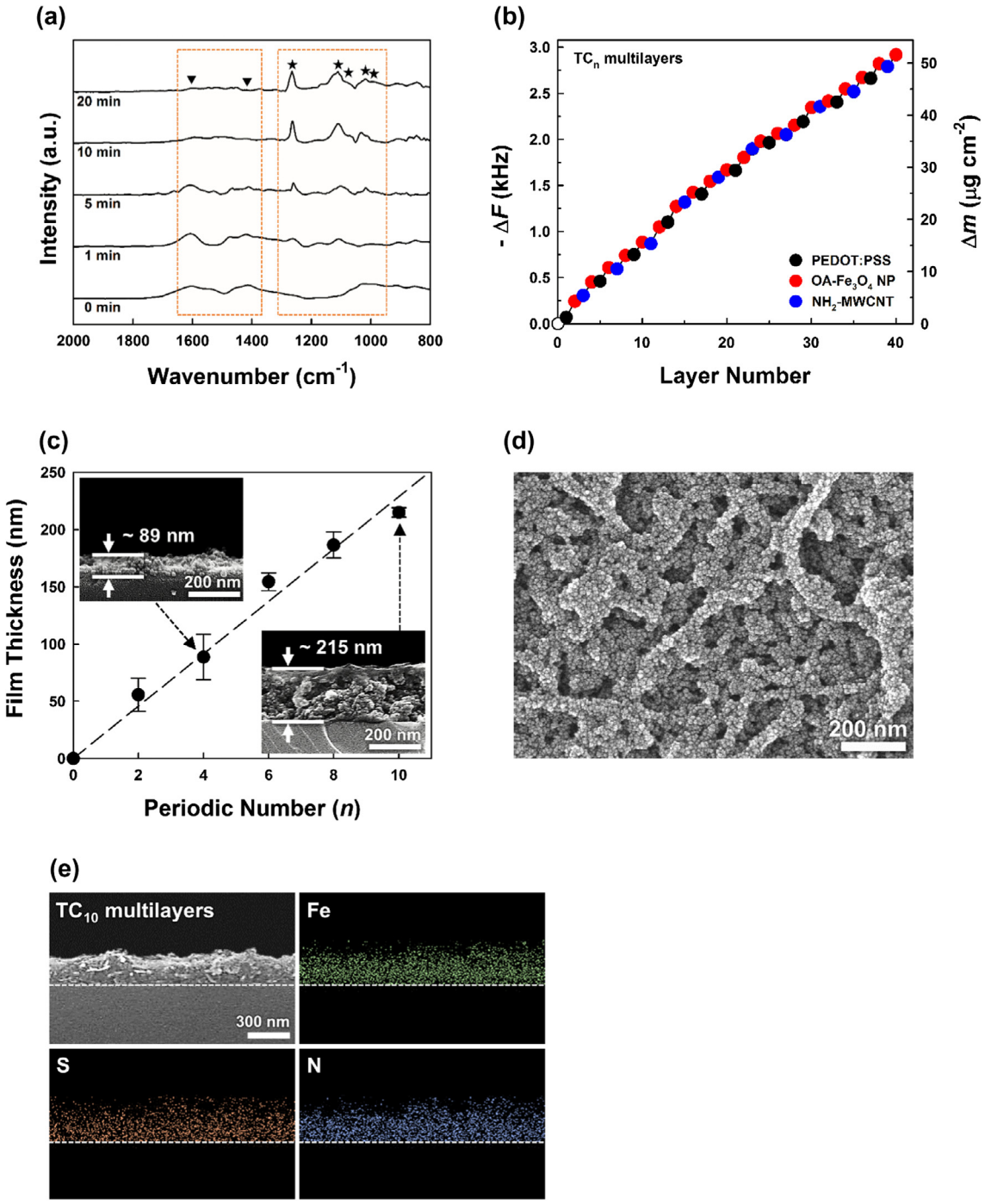

Fig. 1. (a) FTIR spectra of the TC_n multilayers with increasing absorption time of PEDOT:PSS onto the OA-Fe_3O_4 NP-coated films. (b) QCM traces and (c) film thicknesses of the TC_n multilayers as a function of the periodic layer number. Error bars indicate the standard deviation collected by three measurements from cross-sectional FE-SEM images. (d) FE-SEM planar image of the TC_{10} multilayer. (e) Cross-sectional FE-SEM image of the TC_{10} multilayer with EDX elemental mapping images for Fe, S, and N.

values as a function of the scan rate suggests that the designed structure of the TC_n electrode can appropriately balance the charge transfer and pseudocapacitance behaviors compared to other conventional supercapacitor electrodes, including LbL-assembled electrodes (particularly the (OA-Fe_3O_4 NP/NH_2-MWCNT)$_{10}$ electrode) (Fig. 2d). More specifically, the volumetric capacitance value of the amphiphilic TC_{10} electrode was 408 ± 4 F cm^{-3} at 5 mV s^{-1}, which outperformed those of the 81-nm-thick (OA-Fe_3O_4 NP/NH_2-MWCNT)$_{10}$ (241 ± 4 F cm^{-3}) and 105-nm-thick (NH_2-MWCNT/COOH-MWCNT)$_{10}$ electrodes (64 ± 2 F cm^{-3}) at the same scan rate. Additionally, this high volumetric performance of TC_{10} electrodes was also superior to those of the previously reported ternary component-based or LbL-assembled supercapacitor electrodes (Supplementary Information, Table S1). Although the volumetric capacitance of the TC_{10} electrode decreased with an increasing scan rate due to the poor electrochemical kinetics of the Fe_3O_4 NPs [9,10], the TC_n electrodes exhibited high volumetric capacitance value above 200 F cm^{-3} even at a high scan rate of 400 mV s^{-1}. These results evidently imply that the TC_n electrodes with densely packed OA-Fe_3O_4 NP arrays and PEDOT:PSS layers can effectively utilize the high energy density of Fe_3O_4 NPs. Furthermore, PEDOT:PSS within the NH_2-MWCNT matrices mitigates the

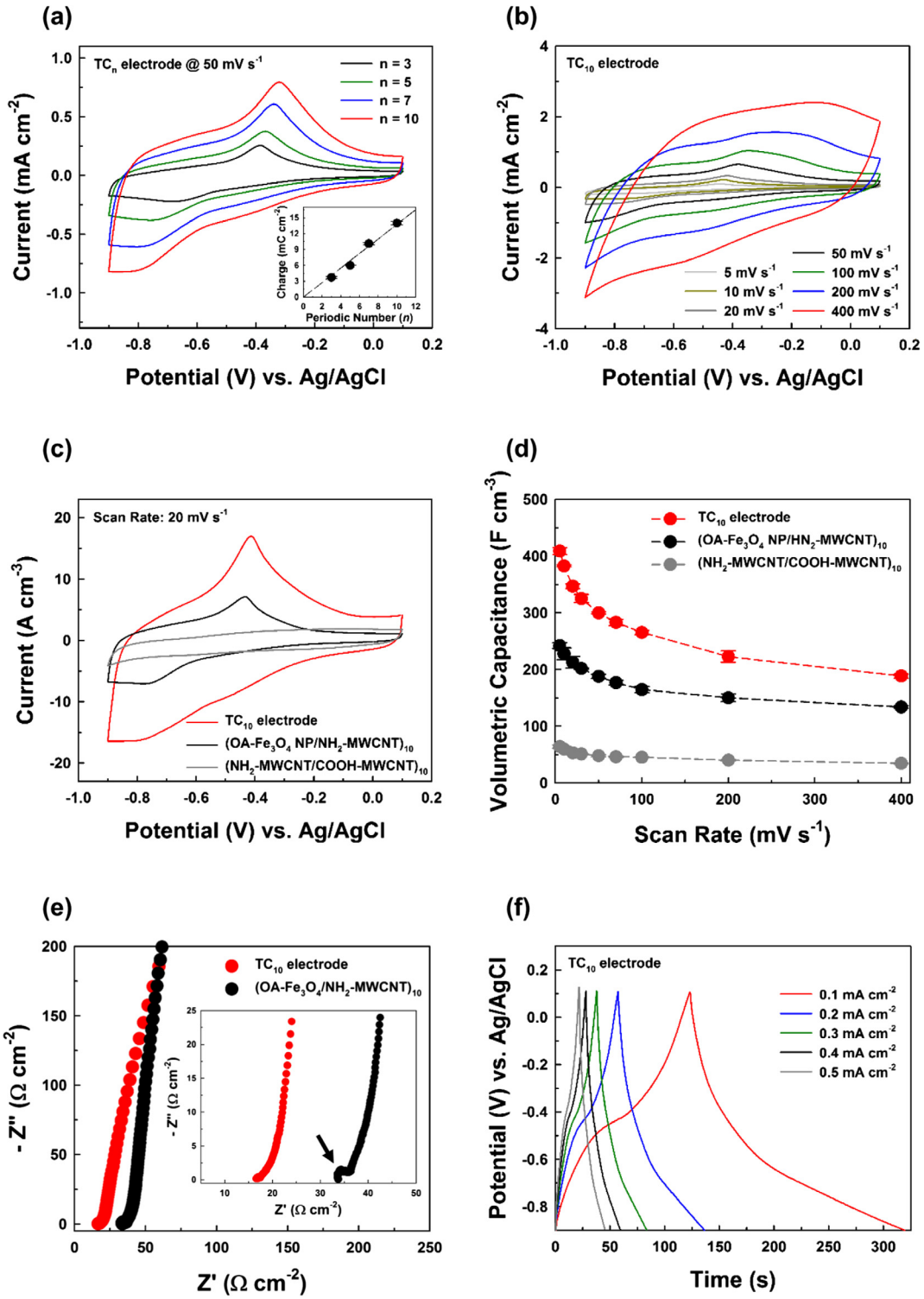

Fig. 2. (a) Cyclic voltammograms of the TC_n multilayer electrodes in 0.1 M Na_2SO_3 as a function of the periodic number (n) ranging from 3 to 10. Inset represents the variation of the total stored charge (in mC cm^{-2}) of the TC_n electrodes with increasing periodic number (n). (b) Scan-rate-dependent cyclic voltammograms of the TC_{10} multilayer electrode measured at 5–400 mV s^{-1}. (c) Comparison of cyclic voltammograms between the TC_{10}, (OA-Fe_3O_4 NP/NH_2-CNT)$_{10}$, and (NH_2-MWCNT/COOH-MWCNT)$_{10}$ electrodes at a scan rate of 20 mV s^{-1}. (d) Volumetric capacitances of the TC_{10}, (OA-Fe_3O_4 NP/NH_2-MWCNT)$_{10}$, and (NH_2-MWCNT/COOH-MWCNT)$_{10}$ electrodes with various scan rates from 5 to 400 mV s^{-1}. (e) Nyquist plots of the TC_{10} and (OA-Fe_3O_4 NP/NH_2-MWCNT)$_{10}$ electrodes. Inset represents the high-frequency region of spectra. (f) GCD profiles of the TC_{10} electrode as a function of the current density from 0.1 to 0.5 mA cm^{-2}.

considerably decreased charge transfer by acting as an additional conductive bridge between neighboring Fe_3O_4 NPs with poor electron conductivity.

Furthermore, we examined the reason for the superior electrochemical performance of the 215-nm-thick TC_{10} electrode compared to that of the multilayer electrode without PEDOT:PSS (i.e.,

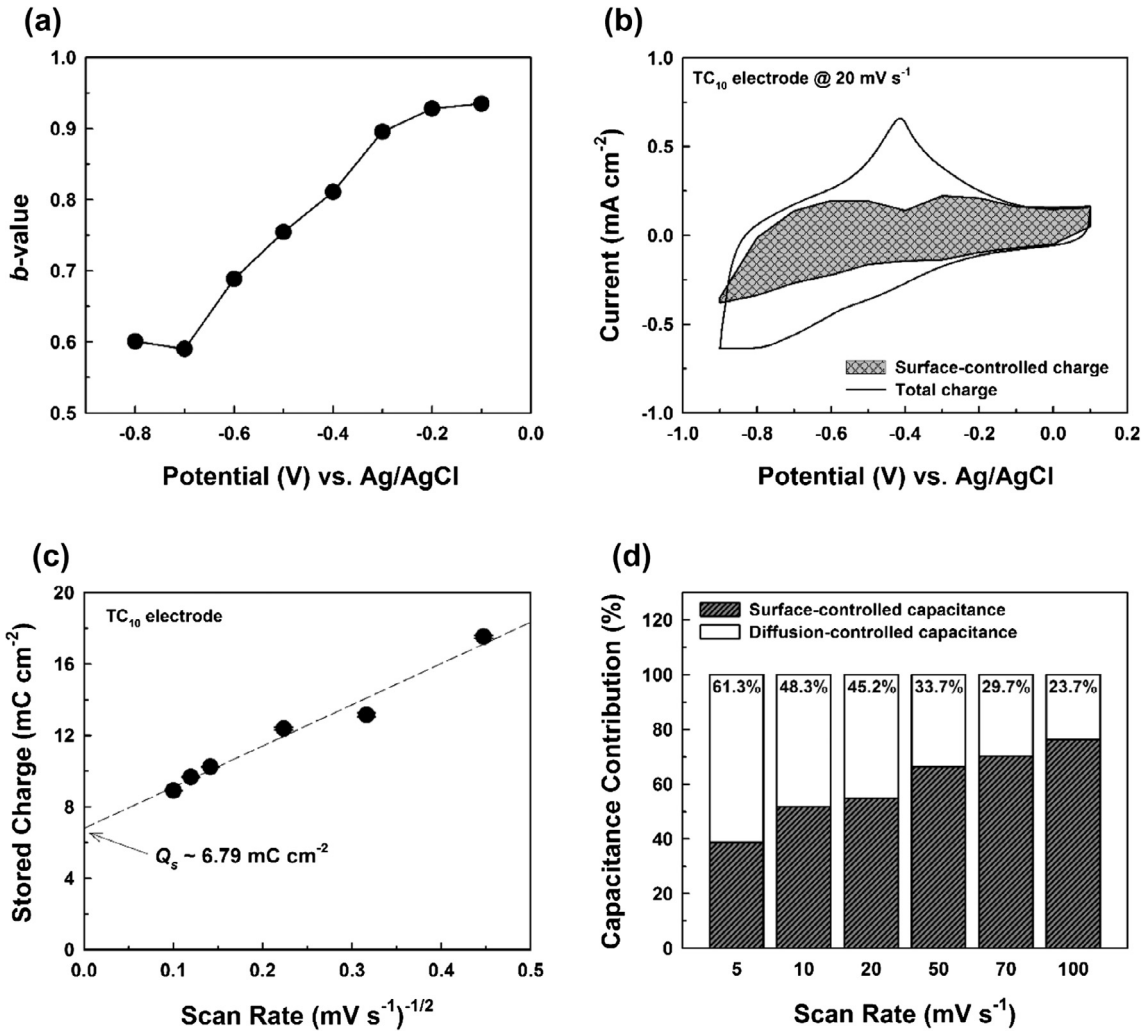

Fig. 3. (a) *b*-Values for the TC_{10} electrode at different potential positions on the cathodic sweep. (b) Cyclic voltammograms of the TC_{10} electrode at a scan rate of 20 mV s^{-1} deconvoluted into the surface- and the diffusion-controlled sections. (c) Plot of the charge vs. scan rate (mV s^{-1}) $^{-1/2}$. The *y*-intercept (Q_s) indicates the surface-controlled charge at a scan rate (v) = ∞. (d) Capacitance contribution of the TC_{10} electrode as a function of the scan rate ranging from 5 to 100 mV s^{-1}.

81-nm-thick (OA-Fe_3O_4 NP/NH_2-MWCNT)$_{10}$ electrode). The equivalent series resistance (ESR) of the TC_{10} electrode was measured to be approximately 16.6 Ω cm^{-2} at the intersection of the real axis in the high-frequency region, which was considerably lower than that of the (OA-Fe_3O_4 NP/NH_2-MWCNT)$_{10}$ electrode (ESR ~ 33.7 Ω cm^{-2}) despite the increased thickness of the TC_{10} electrode (Fig. 2e). Additionally, in contrast to the TC_{10} electrode, the (OA-Fe_3O_4 NP/NH_2-MWCNT)$_{10}$ electrode displayed an evident semicircular arc in this frequency region (arrow in the inset of Fig. 2e), which corresponds to the charge-transfer resistance. This phenomenon indicates the sluggish ion-transfer kinetics due to the large internal resistance within the (OA-Fe_3O_4 NP/NH_2-MWCNT)$_{10}$ electrode [34].

Sequentially, we prepared the TC_n electrodes using PSS with SO_3^- groups (i.e., (PSS/OA-Fe_3O_4 NP/NH_2-MWCNT/OA-Fe_3O_4 NP)$_{10}$) instead of PEDOT:PSS. Despite the nearly identical mass loading of the Fe_3O_4 NPs within the electrodes (~2.35 μg cm^{-2} per layer for the PEDOT:PSS-based electrodes and ~2.45 μg cm^{-2} per layer for the PSS-based electrodes), the CV curve area of the PEDOT:PSS-based TC_{10} electrode was ~26% larger than that of the PSS-based TC_{10} electrode. On the other hand, a smaller peak potential separation (ΔE_p: ~310 mV) between the cathodic (E_{pc}) and anodic peak potentials (E_{pa}) of the PEDOT:PSS-based TC_{10} electrode was observed compared to that of the PSS-based TC_{10} electrode (ΔE_p: ~410 mV) (Supplementary Information, Fig. S6a). Furthermore, the ESR value of the PSS-based TC_{10} electrode was approximately 49.7 Ω cm^{-2} (Supplementary Information, Fig. S6b). These results strongly indicate that the semiconducting PEDOT:PSS polymers inserted within the TC_n electrode can effectively decrease the charge-transfer resistance.

Fig. 2f shows the changes in the GCD curves of the PEDOT:PSS-based TC_{10} electrode with increasing current density from 0.1 to 0.5 mA cm^{-2}. The nonlinear charge-discharge profiles in the potential window from +0.1 to −0.9 V exhibited superimposed redox reactions, which is in accordance with the redox peaks of the CV curves shown in Fig. 2a. For potentials greater than −0.4 V, the time-dependent potential curve showed linear behavior, implying electric double-layer capacitance behavior occurring at the electrode-electrolyte interface. In contrast, at potentials less than −0.4 V, the time dependence of the potential was nonlinear due to the typical pseudocapacitance behavior of the OA-Fe_3O_4 NPs inserted within the TC_{10} electrode. These phenomena are in stark contrast to the linear time-dependent behavior of the H-bonded (NH_2-MWCNT/COOH-MWCNT)$_n$ electrodes without OA-Fe_3O_4 NPs (Supplementary Information, Fig. S7). As a result, this notable charge-storage behavior of the TC_n electrodes was mainly attribu-

ted to the synergetic effect of the high-energy Fe_3O_4 NPs and the electrically conductive components (i.e., PEDOT:PSS and NH_2-MWCNTs).

The total charge-storage mechanisms of pseudocapacitors, such as the TC_n electrodes, can be classified into two types: (1) a diffusion-controlled faradic process via ion intercalation and (2) a surface-controlled process including the faradaic process originating from fast charge transfer at the electrode surface and the non-faradaic double-layer capacitance [12,35,36]. The CV current responses at various scan rate are expressed using the following relation:

$$i = av^b \tag{7}$$

where i and v correspond to the current and scan rate, respectively, and additionally, a and b indicate the variable coefficients. The surface-controlled (i.e., capacitive) reaction, including the pseudocapacitive charge-transfer and double-layer processes, at the electrode surface is proportional to v ($b = 1$), and on the other hand, the diffusion-controlled process is proportional to $v^{1/2}$ ($b = 0.5$).

Based on these various charge-storage mechanisms, we investigated the capacitance contribution of the TC_n electrodes using the CV results. Fig. 30 shows the b-values of the TC_{10} electrode obtained from a log-log plot of the CV current versus the scan rate using the cathodic sweep (Supplementary Fig. S8). The obtained b-values of the TC_{10} electrode were in the range from 0.59 to 0.94, implying that charge storage in the TC_n electrode was induced by both surface- and diffusion-controlled processes [35]. These results are in good agreement with the previous results indicating that charge storage in magnetite originates from both surface redox reactions and intercalation of sulfate and/or sulfite anions [32,37]. From this viewpoint, the CV current of the TC_n electrode at a specific potential can be separated into two components using the following relation [38]:

$$i(\mathrm{V}) = k_1 v + k_2 v^{1/2} \tag{8}$$

where $k_1 v$ and $k_2 v^{1/2}$ represent the surface- and diffusion-controlled storage processes, respectively. The adjustable constants of k_1 and k_2 can be obtained from the slope and y-intercept in the following relation:

$$\frac{i(\mathrm{V})}{v^{1/2}} = k_1 v^{1/2} + k_2 \tag{9}$$

Therefore, for a scan rate of 20 mV s^{-1}, the surface-controlled capacitance was calculated to contribute approximately 54.7% of the total stored charge (i.e., sum of the diffusion- and surface-controlled capacitance, including faradaic reactions at the electrode surface and non-faradaic double-layer capacitance).

The electrochemical charge-storage kinetics of the TC_n electrodes were further analyzed by the relation between the total stored charge and scan rate suggested by Trasatti et al. [39]:

$$Q\ (\text{total charge}) = Q_s + \text{constant}\ (v^{1/2}) \tag{10}$$

where Q_s represents the surface-controlled charge at $v = \infty$, and $v^{-1/2}$ is related to the diffusion-controlled charge.

Fig. 3c shows the total stored charge of the TC_{10} electrode according to the applied scan rate ($v^{-1/2}$). The y-intercept of the linear fit to the data, implying pure surface-controlled charge (Q_s), was measured to be approximately 6.79 mC cm^{-2}. However, as the scan rate decreased, the charge density gradually increased due to the additional diffusion-controlled charge caused by the sufficient reaction time for the full activation of densely packed Fe_3O_4 NPs within the TC_{10} electrode. Correspondingly, the competitive capacitance contribution between the two different charge-storage processes strongly depends on the sweep rate, as shown in Fig. 3d.

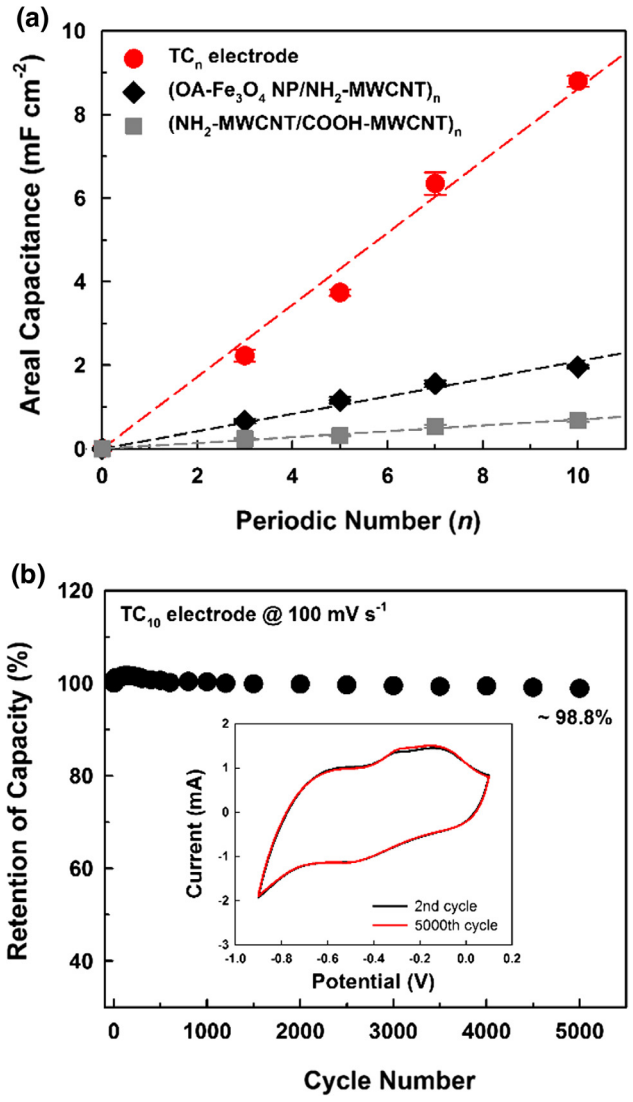

Fig. 4. (a) Areal capacitance of the TC_n, (OA-Fe_3O_4 NP/NH_2-MWCNT)$_n$, and (NH_2-MWCNT/COOH-MWCNT)$_n$ electrodes as a function of the periodic number (n) recorded at 5 mV s^{-1}. (b) Cycling retention of the TC_{10} electrode over 5000 cycles recorded at a constant sweep rate of 100 mV s^{-1}. Inset indicates the CV curves of the TC_{10} electrode at the 2nd and 5000th cycles.

In contrast to the volumetric capacitance, the areal performances of the LbL-assembled electrodes can be further improved by increasing the periodic deposition number (n). As shown in Fig. 4a, the areal capacitances of the LbL-assembled electrodes (i.e., TC_n, (OA-Fe_3O_4 NP/NH_2-MWCNT)$_n$, and (NH_2-MWCNT/COOH-MWCNT)$_n$ electrodes) regularly increased with increasing periodic number (n) at a scan rate of 5 mV s^{-1}. The areal capacitances of the TC_n electrodes reached 8.79 ± 0.06 mF cm^{-2} at a periodic number of 10, outperforming those of the (OA-Fe_3O_4 NP/NH_2-MWCNT)$_{10}$ (1.95 ± 0.03 mF cm^{-2}) and (NH_2-MWCNT/COOH-MWCNT)$_{10}$ (0.67 ± 0.02 mF cm^{-2}) electrodes at the same periodic number. Furthermore, we investigated the long-term cycling performances of the TC_n electrodes. Over 5000 cycles at a scan rate of 100 mV s^{-1}, only 1.2% loss of the initial capacity was observed (Fig. 4b). These results evidently indicate that the amphiphilic TC_n electrodes with covalently bonded interfaces of OA-Fe_3O_4 NP/PEDOT:PSS and OA-Fe_3O_4 NP/NH_2-MWCNTs are highly stable over long-term cycling operation.

Based on these results, for demonstrating the possibility for practical applications, we have further investigated the electrochemical properties of TC_n electrodes in two-electrode working

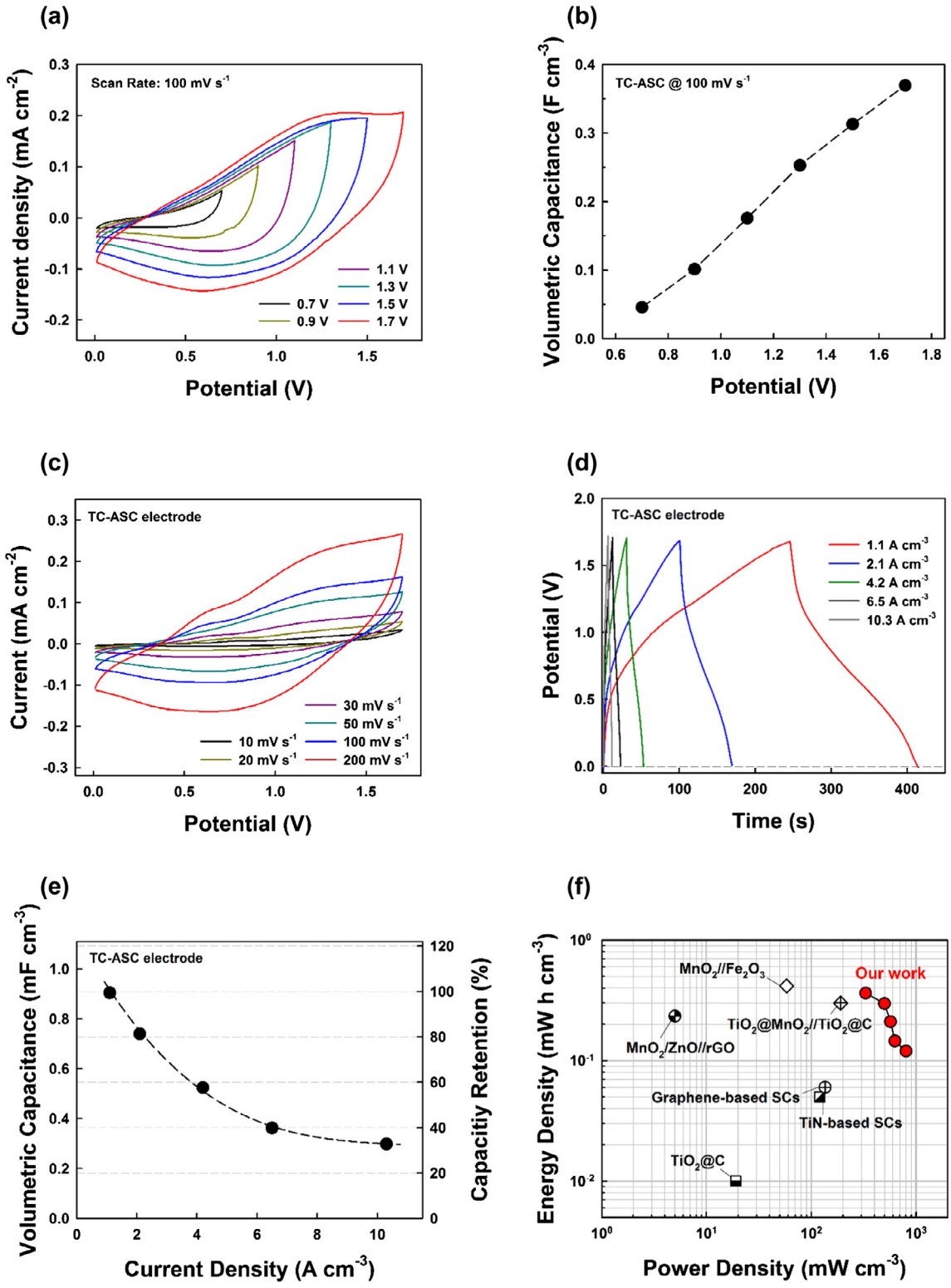

Fig. 5. (a) Potential-dependent CVs and (b) volumetric capacitance of TC-ASCs recorded at a scan rate of 100 mV s^{-1}. (c) CVs of TC-ASCs as a function of scan rate. (d) Change in GCD profiles of TC-ASCs with increasing the current density from 1.1 to 10.3 A cm^{-3}. (e) Change in the volumetric capacitance and capacity retention of TC-ASCs with increasing the current density from 1.1 to 10.3 A cm^{-3}. All data points were obtained from GCD profiles. (f) Ragone plots of TC-ASCs compared with previous reports on volumetric performance.

systems. For this investigation, the ternary component-based asymmetric supercapacitor cells (TC-ASC) were fabricated using Fe_3O_4 NP-based TC_{10} (Fe_3O_4-TC_{10}) and MnO-based TC_{10} (MnO-TC_{10}) electrodes as a negative and a positive electrode, respectively, and then the charge storing features of TC-ASC were evaluated (Fig. 5). In this case, the periodic number (n) of each electrode was adjusted to 10 (Supplementary Fig. S9). Fig. 5a shows the potential-dependent CVs of TC-ASC electrodes at a scan rate of 100 mV s^{-1}. In this case, the regular increase in the area of CV curve with increasing working potential window suggests the typ-

ical and stable capacitive behavior with fast Faradaic reaction of the TC-ASCs in Na_2SO_4 electrolyte. In line with these CVs, the volumetric capacitance was regularly increased up to the working potential of 1.7 V without any irreversible feature, indicating that the charge storage capability of the TC-ASCs can be improved without loss of efficiency (Fig. 5b). Another interesting result is that the CV curves of the TC-ASCs almost maintained their initial curve shape although the scan rate was increased from 10 to 200 mV s^{-1}, implying the good rate performance (Fig. 5c). This capacitive feature can also be seen in GCD profiles with increasing the current density from 1.1 to 10.3 A cm^{-3} (Fig. 5d). The non-linear variation of the potential according to the charging or discharging time implies the pseudocapacitance characteristics originating from PC NPs, which is in good agreement with the CV curves shown in Fig. 5c. Fig. 5e shows the volumetric capacitance and capacity retention performance of the TC-ASCs at the different current densities calculated from discharging time in GCD profiles. In this case, TC-ASCs exhibited the high volumetric capacitance of ~0.91 mF cm^{-3} at a current density of ~1.1 A cm^{-3}, which corresponded to approximately threefold increase compared to the capacitance value (~0.31 mF cm^{-3}) measured at a high current density of ~10.3 A cm^{-3}. This good rate capability of TC-ASCs, in spite of the high mass loading of pseudocapacitive Fe_3O_4 NPs, mainly originate from the porous structure and high conductivity of TC-ASC electrodes as mentioned earlier. As a result, the maximum energy and power densities of TC-ASCs were measured to be ~0.36 mW h cm^{-3} (at 1.1 A cm^{-3}; power density ~0.33 W cm^{-3}) and ~0.82 W cm^{-3} (at 10.3 A cm^{-3}; energy density ~0.30 mW h cm^{-3}), respectively (Fig. 5f), which outperformed the previously reported results [40–45].

4. Conclusion

We demonstrated that amphiphilic TC_n supercapacitor electrodes composed of PEDOT:PSS, NH_2-MWCNTs, and OA-Fe_3O_4 NPs exhibited notable volumetric capacitance with high operational stability. Consecutive ligand exchange reactions between OA loosely bound to the Fe_3O_4 NP surface and the SO_3^- groups of semiconducting PEDOT:PSS as well as between the OA and NH_2 groups of the NH_2-MWCNTs easily changed the densely packed hydrophobic Fe_3O_4 NPs to hydrophilic Fe_3O_4 NPs within the TC_n electrodes. This unique assembly process greatly increased the loading amount of high-energy Fe_3O_4 NPs within the electrodes and, on the other hand, facilitated electrolyte-ion and electron transfer throughout the electrode aided by the porous conductive MWCNT network and semiconducting polymer. Additionally, the areal capacitances of the TC_n electrodes were further improved by increasing the periodic number (n). Furthermore, we successfully fabricated the TC-ASCs based on positive and negative TC_n electrodes, and the formed electrodes exhibited the excellent energy and power densities. Our approach resulted in high energy-storage performance, effectively inducing double-layer- and pseudocapacitance behavior. Given that a variety of electrochemically active materials with extremely different surface polarities can be easily fabricated into thin-film electrodes, we believe that our approach can provide an insight for the design and development of energy-storage electrodes with high volumetric capacitance and scalable areal capacitance through more complex and various heterogeneous components.

Acknowledgements

This work was supported by the National Research Foundation (NRF) grant funded by the Korean government (NRF-2015R1A2A1A01004354).

Appendix A. Supplementary material

Supplementary data associated with this article can be found, in the online version, at https://doi.org/10.1016/j.apsusc.2018.01.153.

References

[1] J.R. Miller, P. Simon, Electrochemical capacitors for energy management, Science 321 (2008) 651–652.
[2] A.S. Arico, P. Bruce, B. Scrosati, J.-M. Tarascon, W.V. Schalkwijk, Nanostructured materials for advanced energy conversion and storage devices, Nat. Mater. 4 (2005) 366–377.
[3] L. Hu, Y. Cui, Energy and environmental nanotechnology in conductive paper and textiles, Energy Environ. Sci. 5 (2012) 6423–6435.
[4] K. Jost, G. Dion, Y. Gogotsi, Textile energy storage in perspective, J. Mater. Chem. A 2 (2014) 10776–10787.
[5] A. Marschilok, C.-Y. Lee, A. Subramanian, K.J. Takeuchi, E.S. Takeuchi, Carbon nanotube substrate electrodes for lightweight, long life rechargeable batteries, Energy Environ. Sci. 4 (2011) 2943–2951.
[6] A.R. Park, J.S. Kim, K.S. Kim, K. Zhang, J. Park, J.H. Park, J.K. Lee, P.J. Yoo, Si–Mn/reduced graphene oxide nanocomposite anodes with enhanced capacity and stability for lithium-ion batteries, ACS Appl. Mater. Interf. 6 (2014) 1702–1708.
[7] S.W. Lee, B.M. Gallant, H.R. Byon, R.T. Hammond, Y. Shao-Horn, Nanostructured carbon-based electrodes: bridging the gap between thin-film lithium-ion batteries and electrochemical capacitors, Energy Environ. Sci. 4 (2011) 1972–1985.
[8] L. Lai, H. Yang, L. Wang, B.K. Teh, J. Zhong, H. Chou, L. Chen, W. Chen, Z. Shen, R. S. Ruoff, J. Lin, Preparation of supercapacitor electrodes through selection of graphene surface functionalities, ACS Nano 6 (2012) 5941–5951.
[9] D. Shin, Y. Ko, J. Cho, Layer-by-layer assembled (high energy carbon nanotube/conductive carbon nanotube)$_n$ nanocomposites for high volumetric capacitance supercapacitor electrodes, RSC Adv. 6 (2016) 21844–21853.
[10] Y. Ko, D. Shin, B. Koo, S.W. Lee, W.-S. Yoon, J. Cho, Ultrathin supercapacitor electrodes with high volumetric capacitance and stability using direct covalent-bonding between pseudocapacitive nanoparticles and conducting materials, Nano Energy 12 (2015) 612–625.
[11] L. Hu, J.W. Choi, Y. Yang, S. Jeong, F. La Mantia, L.-F. Cui, Y. Cui, Highly conductive paper for energy-storage devices, Proc. Natl. Acad. Sci. USA 106 (2009) 21490–21494.
[12] I.E. Rauda, V. Augustyn, B. Dunn, S.H. Tolbert, Enhancing pseudocapacitive charge storage in polymer templated mesoporous materials, Acc. Chem. Res. 46 (2013) 1113–1124.
[13] L. Hu, W. Chen, X. Xie, N. Liu, Y. Yang, H. Wu, Y. Yao, M. Pasta, H.N. Alshareef, Y. Cui, Symmetrical MnO_2–Carbon nanotube–textile nanostructures for wearable pseudocapacitors with high mass loading, ACS Nano 5 (2011) 8904–8913.
[14] Y. Hou, Y. Cheng, J. Liu, Design and synthesis of hierarchical MnO_2 nanospheres/carbon nanotubes/conducting polymer ternary composite for high performance electrochemical electrodes, Nano Lett. 10 (2010) 2727–2733.
[15] S.W. Lee, B.-S. Kim, S. Chen, Y. Shao-Horn, P.T. Hammond, Layer-by-layer assembly of all carbon nanotube ultrathin films for electrochemical applications, J. Am. Chem. Soc. 131 (2009) 671–679.
[16] S.W. Lee, J. Kim, S. Chen, P.T. Hammond, Y. Shao-Horn, Carbon nanotube/manganese oxide ultrathin film electrodes for electrochemical capacitors, ACS Nano 4 (2010) 3889–3896.
[17] M.N. Hyder, S.W. Lee, F.C. Cebeci, D.J. Schmidt, Y. Shao-Horn, P.T. Hammond, Layer-by-layer assembled polyaniline nanofiber/multiwall carbon nanotube thin film electrodes for high-power and high-energy storage applications, ACS Nano 5 (2011) 8552–8561.
[18] W.-H. Khoh, J.-D. Hong, Layer-by-layer self-assembly of ultrathin multilayer films composed of magnetite/reduced graphene oxide bilayers for supercapacitor application, Colloids Surf., A 436 (2013) 104–112.
[19] X. Dong, L. Wang, D. Wang, C. Li, J. Jin, Layer-by-layer engineering Co-Al hydroxide nanosheets/graphene multilayer films as flexible electrode for supercapacitor, Langmuir 28 (2012) 293–298.
[20] K.C. Grabar, K.J. Allison, B.E. Baker, R.M. Bright, K.R. Brown, R.G. Freeman, A.P. Fox, C.D. Keating, M.D. Musick, M.J. Natan, Two-dimensional arrays of colloidal gold particles: a flexible approach to macroscopy metal surface, Langmuir 12 (1998) 2353–2361.
[21] Z. Liang, A.S. Susha, A. Yu, F. Caruso, Nanotubes prepared by layer-by-layer coating of porous membrane templates, Adv. Mater. 15 (2003) 1849–1853.
[22] S. Sun, H. Zeng, D.B. Robinson, S. Raoux, P.M. Rice, S.X. Wang, G. Li, Monodisperse MFe2O4 (M = Fe Co, Mn) nanoparticles, J. Am. Chem. Soc. 126 (2004) 273–279.
[23] J. Park, K. An, Y. Hwang, J. Park, H. Noh, J. Kim, J. Park, N. Hwang, T. Hyeon, Ultra-large-scale synthesis of monodisperse nanocrystals, Nat. Mater. 3 (2004) 891–895.
[24] M. Park, Y. Kim, Y. Ko, S. Cheong, S.W. Ryu, J. Cho, Amphiphilic layer-by-layer assembly overcoming solvent polarity between aqueous and nonpolar media, J. Am. Chem. Soc. 136 (2014) 17213–17223.
[25] Y. Ko, H. Baek, Y. Kim, M. Yoon, J. Cho, Hydrophobic nanoparticle-based nanocomposite films using in situ ligand exchange layer-by-layer assembly and their nonvolatile memory applications, ACS Nano 7 (2013) 143–153.

[26] Y. Kim, K.Y. Lee, S.K. Hwang, C. Park, S.-W. Kim, J. Cho, Layer-by-layer controlled perovskite nanocomposite thin films for piezoelectric nanogenerators, Adv. Funct. Mater. 24 (2014) 6262–6269.
[27] X. Wu, L. Lian, S. Yang, G. He, Highly conductive PEDOT:PSS and graphene oxide hybrid film from a dipping treatment with hydroiodic acid for organic light emitting diodes, J. Mater. Chem. C 4 (2016) 8528–8534.
[28] B. Yameen, M. Ali, M. Álbarez, R. Neumann, W. Ensinger, W. Knoll, O. Azzaroni, A facile route for the preparation of azide-terminated polymers. "Clicking" polyelectrolyte brushes on planar surfaces and nanochannels, Polym. Chem. 1 (2010) 183–192.
[29] L. Zhang, R. He, H.-C. Gu, Oleic acid coating on the monodisperse magnetite nanoparticles, Appl. Surf. Sci. 253 (2006) 2611–2617.
[30] S. Yu, G.M. Chow, Carboxyl group (-CO_2H) functionalized ferromagnetic iron oxide nanoparticles for potential bio-applications, J. Mater. Chem. 14 (2004) 2781–2786.
[31] L. Polito, M. Colombo, D. Monti, S. Melato, E. Caneva, D. Prosperi, Resolving the structure of ligands bound to the surface of superparamagnetic iron oxide nanoparticles by high-resolution magic-angle spinning NMR spectroscopy, J. Am. Chem. Soc. 130 (2008) 12712–12724.
[32] J. Mu, B. Chen, Z. Guo, M. Zhang, Z. Zhang, P. Zhang, C. Shao, Y. Liu, Highly dispersed Fe_3O_4 nanosheets on one-dimensional carbon nanofibers: synthesis, formation mechanism, and electrochemical performance as supercapacitor electrode materials, Nanoscale 3 (2011) 5034–5040.
[33] S.-Y. Wang, K.-C. Ho, S.-L. Kuo, N.-L. Wu, Investigation of capacitance of Fe_3O_4 electrochemical capacitors, J. Electrochem. Soc. 153 (2006) A75–A80.
[34] V. Augustyn, P. Simon, B. Duun, Pseudocapacitive oxide materials for high-rate electrochemical energy storage, Energy Environ. Sci. 7 (2014) 1597–1614.
[35] J. Wang, J. Polleux, J. Lim, B. Dunn, Pseudocapacitive contributions to electrochemical energy storage in TiO2 (anatase) nanoparticles, J. Phys. Chem. C 111 (2007) 14925–14931.
[36] R. Li, Y. Wang, C. Zhou, C. Wang, X. Ba, Y. Li, X. Huang, J. Liu, Carbon-stabilized high-capacity ferroferric oxide nanorod array for flexible solid-state alkaline battery-supercapacitor hybrid device with high environmental suitability, Adv. Funct. Mater. 25 (2015) 5384–5394.
[37] N.-L. Wu, S.-Y. Wang, C.-Y. Han, D.-S. Wu, L.-R. Shiue, Electrochemical capacitor of magnetite in aqueous electrolytes, J. Power Source 113 (2003) 173–178.
[38] T.-C. Liu, W.G. Pell, B.E. Conway, Behavior of molybdenum nitrides as materials for electrochemical capacitors, J. Electrochem. Soc. 145 (1998) 1882–1888.
[39] S. Ardizzone, G. Fregonara, S. Trasatti, "Inner" and "Outer" active surface of RuO_2 electrodes, Electrochim. Acta 35 (1990) 263–267.
[40] Y. Xu, Z. Lin, X. Huang, Y. Liu, Y. Huang, X. Duan, Flexible solid-state supercapacitors based on three-dimensional graphene hydrogel films, ACS Nano 7 (2013) 4042–4049.
[41] X. Lu, G. Wang, T. Zhai, M. Yu, S. Xie, Y. Ling, C. Liang, Y. Tong, Y. Li, Stabilized TiN nanowire arrays for high-performance and flexible supercapacitors, Nano Lett. 12 (2012) 5376–5381.
[42] H. Zheng, T. Zhai, M. Yu, S. Xie, C. Liang, W. Zhao, S. Wang, Z. Zhang, X. Lu, TiO2@C core-shell nanowires for high performance and flexible solid-state supercapacitors.-based electrodes, J. Mater. Chem. C 1 (2013) 225–229.
[43] X. Lu, Y. Zeng, M. Yu, T. Zhai, C. Liang, S. Xie, M. Balogun, Y. Tong, Oxygen-deficient hematite nanorodes as high-performance and novel negative electrodes for flexible asymmetric supercapacitors, Adv. Mater. 26 (2014) 3148–3155.
[44] X. Lu, M. Yu, G. Wang, T. Zhai, S. Xie, Y. Ling, Y. Tong, Y. Li, H-TiO_2@MnO_2//H-TiO_2@C core-shell nanowires for high performance and flexible asymmetric supercapacitors, Adv. Mater. 25 (2013) 267–272.
[45] Z. Wang, Z. Ahu, J. Qiu, S. Yang, High performance flexible solid-state asymmetric supercapacitors from MnO_2/ZnO core-shell nanorods//specially reduced graphene oxide, J. Mater. Chem. C 2 (2014) 1331–1336.